J Mater Sci: Mater Electron (2021) 32:28618–28632

Influence of CIGS film thickness on the microstructure, bulk optoelectronic, and surface electrical properties

Narendra Bandaru[1] and Emila Panda[1,*]

[1] *Department of Materials Science and Engineering, Indian Institute of Technology Gandhinagar, Palaj, Gujarat 382355, India*

Received: 10 June 2021
Accepted: 12 October 2021
Published online: 23 October 2021

ABSTRACT

The present work addresses the changing microstructure, bulk optoelectronic, and surface electrical properties of sputter deposited Cu(In,Ga)Se_2 (CIGS) films on the soda lime glass (SLG) substrates as a function of altered film thickness. To this end, these films were deposited by varying the deposition time from 180 to 540 min in radio frequency (RF) magnetron sputtering and by using a low substrate temperature of 523 K. A range of experimental techniques were then used to investigate the microstructure, bulk optoelectronic, and surface electrical properties of these films. All these films are found to grow in single phase, chalcopyrite crystal structure, and with dominant (112) orientation, though the overall composition of these films is found to slightly alter. Moreover, a semimetallic to semiconductor transition in the thickening CIGS film is seen, which is then correlated with their hole concentration. Based on these observations and the positions of the Fermi energy, a possible theory regarding the presence of the types, quantities, and positions of the electronic defect states and their variations by thickening the CIGS film is discussed. Both the transport and optical band gaps (E_g) are found to follow the same trend, which could also be related with the compositional variation in these films. Moreover, CIGS film deposited for 540 min is found to yield a film thickness of about 2.85 μm, with hole concentration of 2.17×10^{17} cm^{-3} and optical band gap of 1.16 eV; optoelectronic properties appropriate for an absorber layer in photovoltaic application.

1 Introduction

Cu-based chalcopyrite material, Cu(In,Ga)Se_2 (CIGS) is a I–III–VI_2 semiconductor compound, which is being extensively studied as one of the absorber materials due to its high absorption coefficient ($> 10^5$ cm^{-1}), direct and tunable optical band gap (1.04–1.67 eV) by varying the In/Ga-ratio, high conversion efficiency, long-term-stability, and potential for cost-effective power generation [1–3]. Note here that, among all other available technologies, technologies involving thin film solar cell is promising because of the use of reduced material cost (due to the use of less material) and possibility of in-line

Address correspondence to E-mail: emila@iitgn.ac.in

https://doi.org/10.1007/s10854-021-07238-x

production [4–6]. However, one of the major disadvantages of thin film solar cells as compared to those of the monocrystalline ones is the presence of higher defect densities, which significantly increase the carrier recombination, thereby adversely affecting their efficiencies [6]. Out of all the polycrystalline semiconductor materials that are available in the literature, CIGS is promising because of its electrically inactive grain boundaries and high efficiency (23.4%) [7–10]. Moreover, these solar cells can be competitive in the PV industry owing to their significant advantages, like minimal absorber material usage with fewer processing steps, and use of inexpensive substrates (i.e., soda lime glass (SLG), polyimide, and/or metal foils), which could lower the overall manufacturing cost [11]. Furthermore, these solar cells can be made in building-integrated and portable applications, in addition to their terrestrial applications [12–15]. In addition to above, these solar cells exhibit high radiation resistance compared to other solar cell technologies consisting of crystalline silicon and III–V semiconductors and thus are more suitable for space applications [16]. Apart from solar cell applications, CIGS thin films are also used in thin film transistor applications (TFTs) and as photo-electrodes in photoelectrochemical cells (PEC) for hydrogen production [17–20].

Note that, thickness of an absorber layer plays a significant role in the fabrication of an efficient, cost-effective solar cell device [21, 22]. Whereas the maximum thickness of the CIGS-based absorber layer is limited to only few micrometers (of up to 4 μm) owing to its higher absorption coefficient and direct band gap, that of its counterpart, silicon-based solar cells need at least few hundreds of micrometer thickness (of the order of 200–300 μm) [23]. Reducing the absorber layer thickness leads to significant reduction in the device efficiency because of a cumulative effect of insufficient absorption of the solar energy and recombination of minority carriers (i.e., electrons) at the back contact surface. Similarly its thickness higher than optimum is unreasonable because of increased material consumption. Hence, an optimum absorber layer thickness, which maximizes the open circuit voltage (V_{oc}), short circuit current (I_{sc}), and fill factor (FF) is needed for fabricating an efficient solar cell device [22, 24, 25]. Note here that, a change in composition to optimize the optical band gap (and also thickness) of this film also alters the electronic defect states, thereby modifying both the surface and bulk electrical properties [26–28]. Optimizing these optoelectronic properties is crucial for making efficient solar cells. Moreover, it is important to understand the surface electrical properties of these films as this film is usually present in a stack, hence influencing the microstructure and optoelectronic properties of the next layers and thereby the entire device [29, 30].

Though a wide range of deposition techniques (i.e., vacuum, and non-vacuum) are being used to synthesize CIGS films, for low-cost synthesis, one step sputtering, or the electrochemical deposition might be promising [31–37]. Though single step electrodeposition technique has several advantages, like, large area deposition, and cheaper capital expenditure, electrodeposition of quaternary alloys could be tricky because of the differences in the deposition potential of the precursors, which might then require precise control of various process parameters (i.e., chemical composition of the deposition bath (i.e., concentration of the ions), the pH, the nature of the substrate surface state, the electrolyte type, the applied current density.) for depositing a single-phase CIGS film [38–40].

In this regard, the present work addresses the variation in the microstructure, bulk optoelectronic, and surface electrical properties of a thickening CIGS film deposited by varying the deposition time from 180 to 540 min in single step radio frequency (RF) magnetron sputtering. Following the deposition, a wide range of experimental techniques were used to investigate the microstructure, bulk optoelectronic, and surface electrical properties of these films. Unlike the conventional route, here the deposition process was carried out in a single step from a quaternary CIGS target and by keeping the substrate temperature relatively lower (i.e., 523 K). Moreover, no post-deposition annealing and/or selenization treatment was conducted here, which make this deposition route facile, environment friendly, and cost-effective. Moreover, sputtering is a scalable technique and results in the fabrication of a high quality film along with high adherence with that of the substrate [41]. Most of the work toward fabricating high quality CIGS in sputtering are either based on the deposition from multiple targets at a higher substrate temperature of > 823 K, followed by selenization treatment using toxic H_2Se again at a relatively higher temperature of > 823 K or deposition using co-evaporation route [42–47]. While the former involves two step

deposition process and has environment concerns, the latter is an expensive route to commercialize. Moreover, to the best of our knowledge, the thickness dependent alteration in the microstructure, bulk optoelectronic, and surface electrical properties of these films could not be found in the literature, which is crucial to understand and optimize the film thickness for photovoltaic application.

2 Experimental procedure

Series of CIGS thin films were deposited on ultrasonically cleaned SLG substrates by varying the deposition time (t) from 180 to 540 min in RF magnetron sputtering. Single quaternary CIGS target with 99.999% purity (of 2-in. diameter and 3 mm thick, which was bonded with a copper back plate by means of indium metal) was used here as the sputtering target. The elemental composition of this CIGS target (in at.%) was Cu: 25, In: 17.5, Ga: 7.5, and Se: 50. Prior to film deposition, the chamber was evacuated to 5×10^{-5} mbar pressure with the help of a turbo molecular pump backed by a rotary pump, after which high purity (99.999%) Argon gas was introduced as the working gas for the sputter deposition process. The optimized process parameters used here were 523 K substrate temperature (T_{sub}), 90 W rf power, 40 sccm Argon gas flow rate, 15 rpm substrate rotation, and 7.0 cm substrate-to-target distance. Prior to each deposition, the CIGS target was pre-sputtered for 15 min to remove the surface contaminants present on its surface.

After deposition, a range of characterization techniques were used to assess the microstructure and optoelectronic properties of these films. The phase, crystallinity, and crystallite size of these films were determined using grazing incident X-ray diffractometer (GIXRD; *Model: D8 Discover, Supplier: Bruker Corporation*) at an optimized grazing angle of 3° and in the 2θ range of 20°–90° (step size of 0.02°) using Cu K_α (λ = 0.15418 nm) radiation. The thicknesses along with the uniformity of these prepared films were ascertained by using cross-sectional field emission scanning electron microscope (FESEM; *Model: JSM 7600 F, Supplier: JEOL Ltd.*). The composition of these deposited films was studied using energy dispersive X-ray, which is attached with the FESEM (EDS, *Model: AZtec, Supplier: Oxford Instrument*). Electrical properties of these films which consist of electrical resistivity (ρ), carrier (or hole) concentration (p_h), and carrier mobility (μ_h) were determined by using Hall effect measurement system at room temperature in the Van der Pauw configuration (*Model: 5300 series HEMS, Supplier: Ecopia*). Optical properties which consist of transmittance, reflectance, and optical band gap were measured using UV–Vis-NIR spectrophotometer (*Model: Carry 5000, Supplier: Agilent*) in the wavelength range of 300–2200 nm. X-ray photoelectron spectroscopy (XPS; *Model: PHI 5000, Versa Prob II, Supplier: ULVAC-PHI, Inc.*) with a spot size of 10 μm was employed to investigate the surface chemical states of various elements present in these films. Scanning tunneling microscopy (STM)/scanning tunneling spectroscopy (STS) analyses were performed at room temperature under ambient condition using the attached STM module of the scanning probe microscope (SPM; *Model: NanoScope Multimode 8.0, Supplier: Bruker Corporation*). To this end, first STM images were captured using Pt/Ir tip (*PT-10*) of 0.25 mm diameter and 8 mm length. Then local current–voltage (I–V) patterns were recorded from 17 different locations of these individually captured 2 μm × 2 μm STM images by applying constant set current of 1.5 nA while varying the sample bias in the range of −1.0 to + 1.0 V.

3 Results and discussion

An increase in t from 180 to 540 min was found to increase the CIGS film thickness from 901 ± 37.35 nm to 2845 ± 35.27 nm (see Fig. 1a–e). Moreover, these films were found to be uniformly thick, crack free, polycrystalline, and exhibits strong (112) orientation along with minor (220) peak, which are in agreement with the standard profile of CIGS chalcopyrite structure (JCPDS card File: 35-1102; see Figs. 1a–e, 2a and Ref. [48–50]. Note that, as observed in the obtained XRD spectra, the intensity of the (220) peak is relatively low compared to that of the (112) plane and could be associated to the lower surface energy of (112) orientation [51]. The degree of the preferred orientation in these films can be quantified using their diffractions line ratios, i.e., R_I, defined as the ratio of the diffraction intensity of (112) peak to the sum of the intensities of all the diffraction peaks in the XRD patterns.

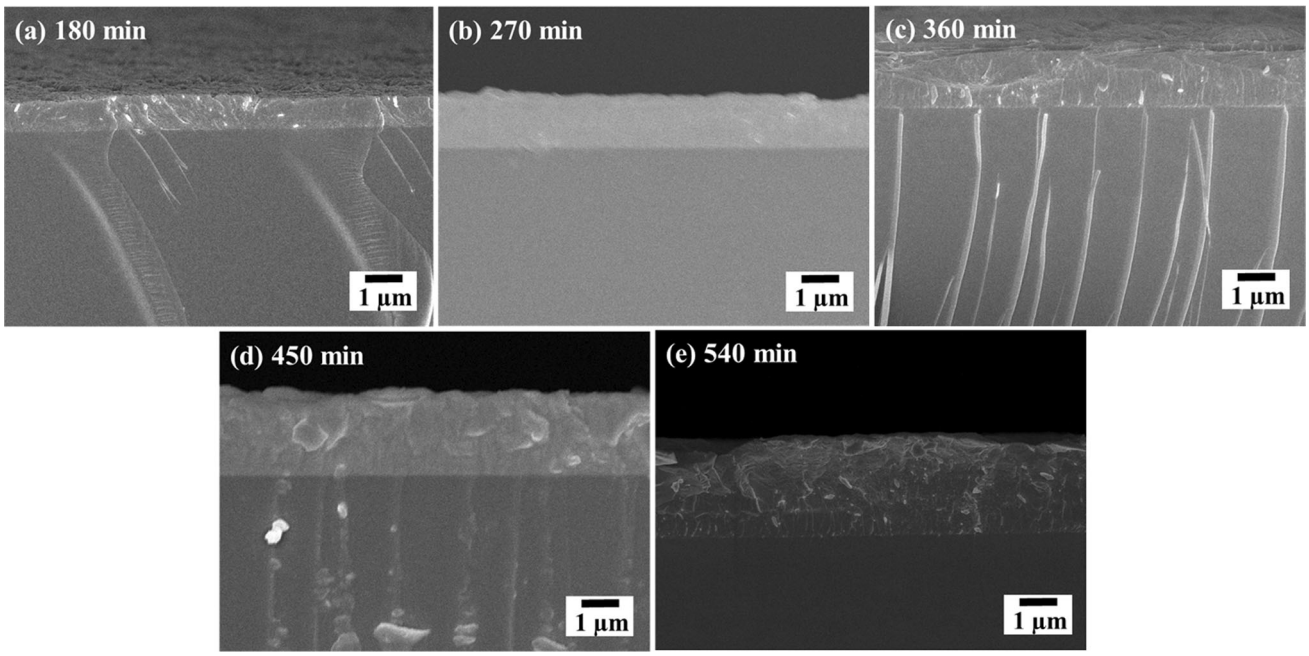

Fig. 1 **a**–**e** Cross-section FE-SEM images for the CIGS films deposited on the soda lime glass substrates by varying deposition time from 180 to 540 min using RF magnetron sputtering

$$R_{\mathrm{I}} = \frac{I_{(112)}}{\sum_{\mathrm{allpeaks}} I_{(hkl)}}, \tag{1}$$

where $I_{(\mathrm{hkl})}$ is the intensity of (*hkl*) peak [52]. The calculated intensity ratio value for R_{I} (112) was found to increase from 0.94 to 0.99 with increasing film thickness (see Fig. 2b), indicating (112) as the obtained diffraction pattern in these films [53, 54]. No extra peaks in the XRD spectra corresponding to the metallic or any other complex phases were observed, indicating growth of single-phase CIGS for all cases. Film crystallinity was found to improve with increasing thickness. Subsequently, the average crystallite size (*D*) in (112) orientation which was calculated using the following Scherrer equation was found to increase from 9.3 to 16.04 nm with increasing film thickness (see Fig. 2b) [55, 56].

$$D = \frac{0.9 \cdot \lambda}{\beta \cos \theta}, \tag{2}$$

where *D* is the crystallite size, λ is the wavelength of the incident X-ray (λ = 0.15406 nm), β is the line broadening in radians measured as the full-width at half-maximum (FWHM), and θ is the Bragg angle of diffraction peak.

The local surface electrical properties (i.e., *I*–*V*), as measured using STS from 17 different locations of the thickening CIGS films along with their averages are plotted in Fig. 3a–e. Further, their corresponding tunneling conductance (*dI*/*dV*) (i.e., obtained by differentiating the measured *I*–*V* curves) which represent the local density of states (LDOS) of the sample (ρ_{sample}) are presented against the bias voltage (V) in Fig. 3a′–e′.

From *I*–*V* characteristics, the measured tunneling conductance (*dI*/*dV*) of the thickening CIGS films are related as per the following equation:

$$\frac{\mathrm{d}I}{\mathrm{d}V} \propto e\rho_{\mathrm{sample}}(eV)\rho_{\mathrm{tip}}(0)T(E, eV, d), \tag{3}$$

where *e* is the electronic charge, *V* is the bias voltage, ρ_{tip} is the local density of states of the tip, at an electron energy *E* from the fermi energy of the sample E_{F} and $T(E, eV, d)$ is the tunneling transmission probability for electrons with energy *E* and applied voltage *V* over the distance between the sample to the tip *d*. Assuming the effects of ρ_{tip} and $T(E, eV, d)$ to be minimal and often neglected in the literature, d*I*/d*V* can be directly proportional to only ρ_{sample} [57–60].

The local surface electrical properties (i.e., *I*–*V*) from a particular sample surface were found to be almost similar in nature, indicating electrically homogeneous sample surface, though electrical heterogeneity was seen among the thickening CIGS films deposited at varying *t*. The gap between the

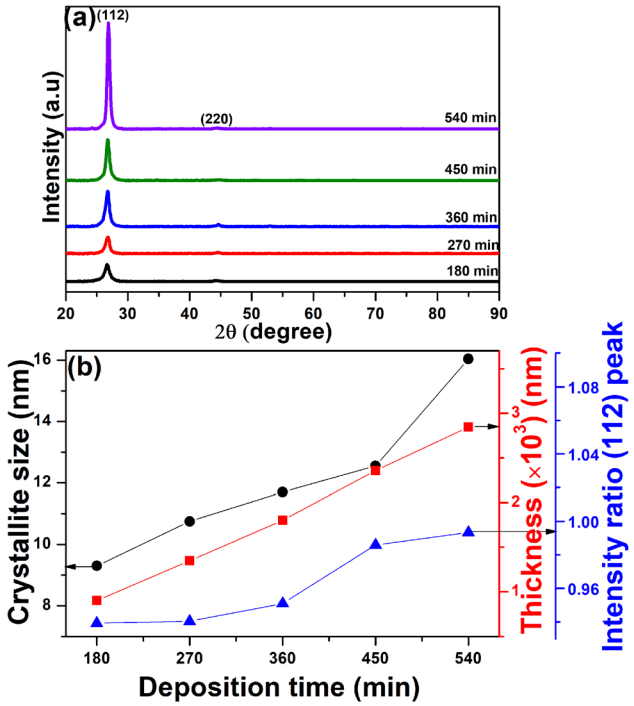

Fig. 2 **a** X-ray diffraction pattern and **b** variation in crystallite size, film thickness for the CIGS films deposited on the soda lime glass substrates by varying deposition time from 180 to 540 min using RF magnetron sputtering

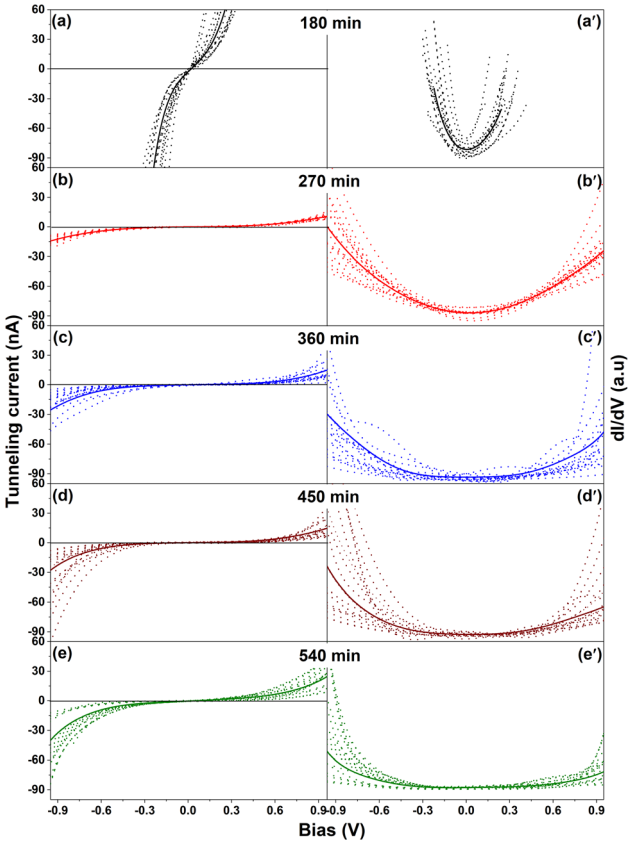

Fig. 3 Average (solid line) and individual (dotted lines) tunneling current (I) vs bias voltage (V) **a**–**e**; and dI/dV curves **a′**–**e′** as measured using STM/STS for the CIGS films deposited on the soda lime glass substrates by varying deposition time from 180 to 540 min using RF magnetron sputtering

conduction band edge (CBE) and the valence band edge (VBE; i.e., zero conductance around the Fermi energy) is defined as the transport bandgap and was calculated as the energy difference between the first inception in the positive and that of in the negative voltage sides of the dI/dV curves [57–59]. The CIGS films deposited at lower t of 180 and 270 min showed non-zero conductance region around the Fermi level indicating their semi-metallic nature (see Fig. 3a, b, a′, and b′) [60]. However, with increasing film thickness (i.e., for the films deposited at t of 360 to 540 min), non-conductance around the Fermi level was observed, a behavior typical for the semiconducting materials and found to be 1.13 ± 0.04, 1.10 ± 0.06, and 1.04 ± 0.06 eV for the films deposited at 360, 450, and 540 min, respectively [61, 62]. Monig et al. had found out an averaged surface bandgap of (1.4 ± 0.2) eV from the grains of the CIGS film with the VBE and CBE being (−0.67 ± 0.1) and (0.87 ± 0.1) eV, respectively [63]. In another work, Chakrabarti et al. had discussed the shifting in the transport band gap and its relation to the change in the positions of CBE and VBE in ultrathin CZTS nanocrystal films [64]. Additionally, asymmetry between the positive and negative bias regions for these three thicker films was seen, in particular the Fermi level being found closer to the valence band edges than those of the conduction band edges of these films (see Figs. 3c, d, c′, d′, and 4).

Though semi-metallic behavior is an indication of the presence of continuous energy states within the band gap of the material, which can be related to the existence of large number and types of electronic defect states (i.e., V_{Se}, Ga_{Cu}, Cu_i, Cu_{Se} as donor types and Cu_{In}, V_{Cu}, V_{In} as acceptor type defect states), a semiconducting behavior with a Fermi energy closer to the valence band edge indicates the presence of relatively larger number of acceptor type of defect states [65–69]. However, the observed p-type characteristic in HEMS for all these CIGS films irrespective of their thicknesses suggested the presence of higher

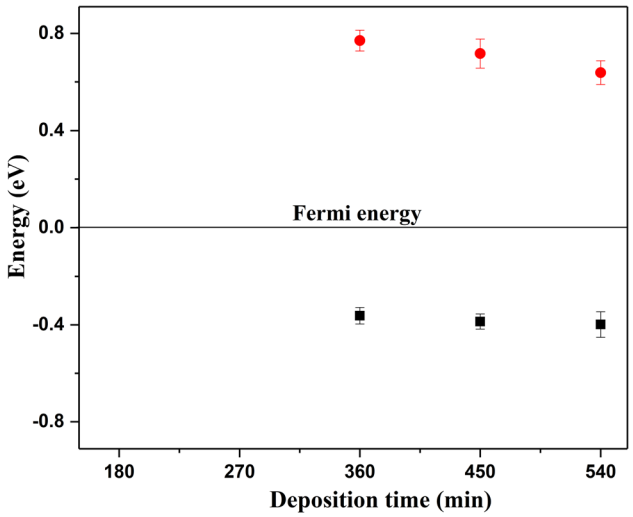

Fig. 4 Positions of the conduction band edge and valence band edge as measured using STM/STS for the CIGS films deposited on the soda lime glass substrates by varying deposition time from 180 to 540 min using RF magnetron sputtering

quantities of acceptor types of defect states in these films. Moreover, p_h was found to be very high (i.e., 2.61×10^{20} cm^{-3}) for the CIGS film deposited at the shortest time (i.e., the thinnest film), which continuously decreased with increasing film thickness (i.e., to 2.17×10^{17} cm^{-3}) for the film deposited at t of 540 min (see Fig. 5). This implied that, the number of acceptor types of defect states was highest for the film deposited at lowest t, the concentration of which decreased with increasing t. Accordingly, the separation distance between the Fermi energy and the valence band edge was found to increase with increasing CIGS film thickness (only for the semiconductor films; see Fig. 4 and Table 3). A. Bera et al. had studied the dI/dV spectra on CdS and CdTe nanostructures and showed the shift in the transported gap from the broken and continuous lines which are indicating conduction- and valence band-edges in the applied positive and negative voltages, respectively [70]. S. Broker et al. studied the STS characteristics to the Na-free absorbers, the Cu-rich and KCN etching for the CIGSe films. They observed the significant changes in the Cu-rich grown materials compared to the Na-free absorbers and KCN etching treatment films [71]. In another study, Li et al. discussed and estimated the surface band gap by using the band edge positions obtained from dI/dV spectras and their results showed the band gap movements with respect to the fermi level in the CIGS films [72].

Note that, XPS measurements lead to the identification of the changes in the chemical bonding states for various elements. To this end, the spectral lines of Cu 2p, In 3d, Ga 2p, and Se 3d for all these deposited films were measured in the range of 925 to 960 eV,

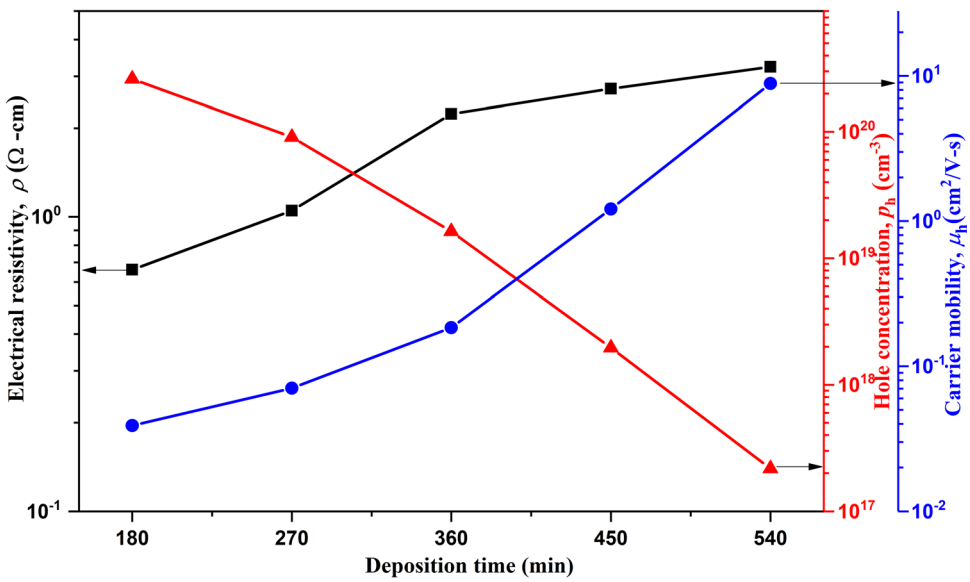

Fig. 5 Variation in electrical resistivity (ρ), carrier concentration (p_h), and carrier mobility (μ_h) as measured using HEMS for the CIGS films deposited on the soda lime glass substrates by varying deposition time from 180 to 540 min using RF magnetron sputtering

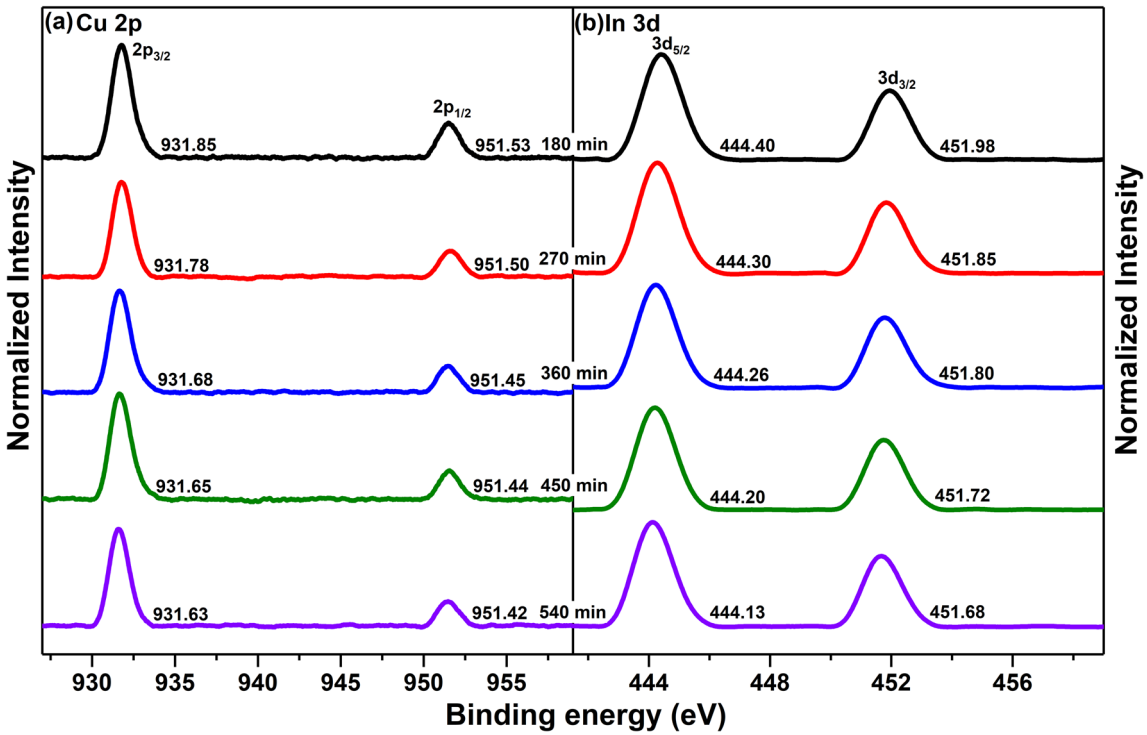

Fig. 6 Core level XPS spectra of **a** Cu 2p and **b** In 3d for the CIGS films deposited on the soda lime glass substrates by varying deposition time from 180 to 540 min using RF magnetron sputtering

440 to 470 eV, 1110 to 1140 eV, and 40 to 65 eV, respectively, which are presented in Figs. 6 and 7 along with their binding energy positions in Table 1. All these measured high resolution spectra of Cu 2p, In 3d, Ga 2p, and Se 3d peak positions were referenced with respect to the binding energy of the impurity C 1s line (284.6 eV).

Doublet splitting of Cu 2p spectral lines was observed for all these films, with average binding energy positions of Cu $2p_{3/2}$ and $2p_{1/2}$ being 931.71 ± 0.08 and 951.48 ± 0.02 eV, respectively, along with their separation distances of about 19.77 ± 0.06 eV, data consistent with the standard XPS reference spectrum for Cu in CIGS, suggesting the valence state of Cu as Cu^{1+} [73–76]. Doublet splitting of In 3d spectral lines was observed for all these films, with average binding energy positions of In $3d_{5/2}$ and $3d_{3/2}$ being 444.25 ± 0.09 and 451.80 ± 0.01 eV, respectively, along with their separation distances of about 7.55 ± 0.18 eV, which are characteristic of In^{3+} and are in agreement with the data reported for In in CIGS [75, 77]. The peak corresponding Ga $2p_{3/2}$ was found at 1117.23 ± 0.01 eV, which was characteristic of Ga in + 3 valence state [77, 78]. Se spectra showed Se $3d_{5/2}$ and $3d_{3/2}$ peaks at 53.25 ± 0.09 and 54.16 ± 0.06 eV, respectively, with a separation distance of 0.91 ± 0.04 eV, confirming the valence state of Se as -2 [79, 80]. Moreover, the chemical composition of these CIGS films was then calculated by analyzing the XPS spectrum and by using the following equation:

$$C_{Cu} = \frac{I_{Cu}/S_{Cu}}{\sum_i I_i/S_i}, \quad (4)$$

where C_{Cu} is Cu atomic concentration, I_{Cu} and I_i are the area under the curve of Cu and the other elements, S_{Cu} and S_i are relative sensitivity factors of Cu and other elements. Similar calculations were carried out for other elements present in these films (i.e., In, Ga, and Se) [81]. Note that for accurate data estimation, SEM–EDS measurements were carried out at ten different locations on each sample, following which an average and standard deviation values were obtained.

Based on the reports presented in the literature, Cu_{In}, V_{Cu}, and V_{In} are the shallow acceptor type of electronic defect states, which are usually present in a

CIGS film because of their lower formation energies of the order of − 0.5, 0.6, and 1.1 eV, respectively [65]. Thus the thinnest CIGS film (i.e., the film deposited at t of 180 min) can be speculated to have the maximum concentration of these three shallow acceptor level electronic defect states. However, this film was found to have the maximum copper and minimum indium concentrations out of all the samples deposited here (see XPS and SEM–EDS data in Table 2, Figs. 8 and 9), which implied the presence of large quantities of Cu_{In} and V_{In} (apart from Cu and In in their lattice sites). With increasing film thickness, Cu concentration was found to decrease with an increase in the In quantities, which would have reduced both the quantities of Cu_{In} and V_{In} type of acceptor defects, thereby reducing p_h in these films (see Fig. 5).

Moreover, with increasing film thickness, the donor-related electronic defect states (i.e., V_{Se}, Ga_{Cu}, Cu_i, Cu_{Se}) were found to reduce because of an

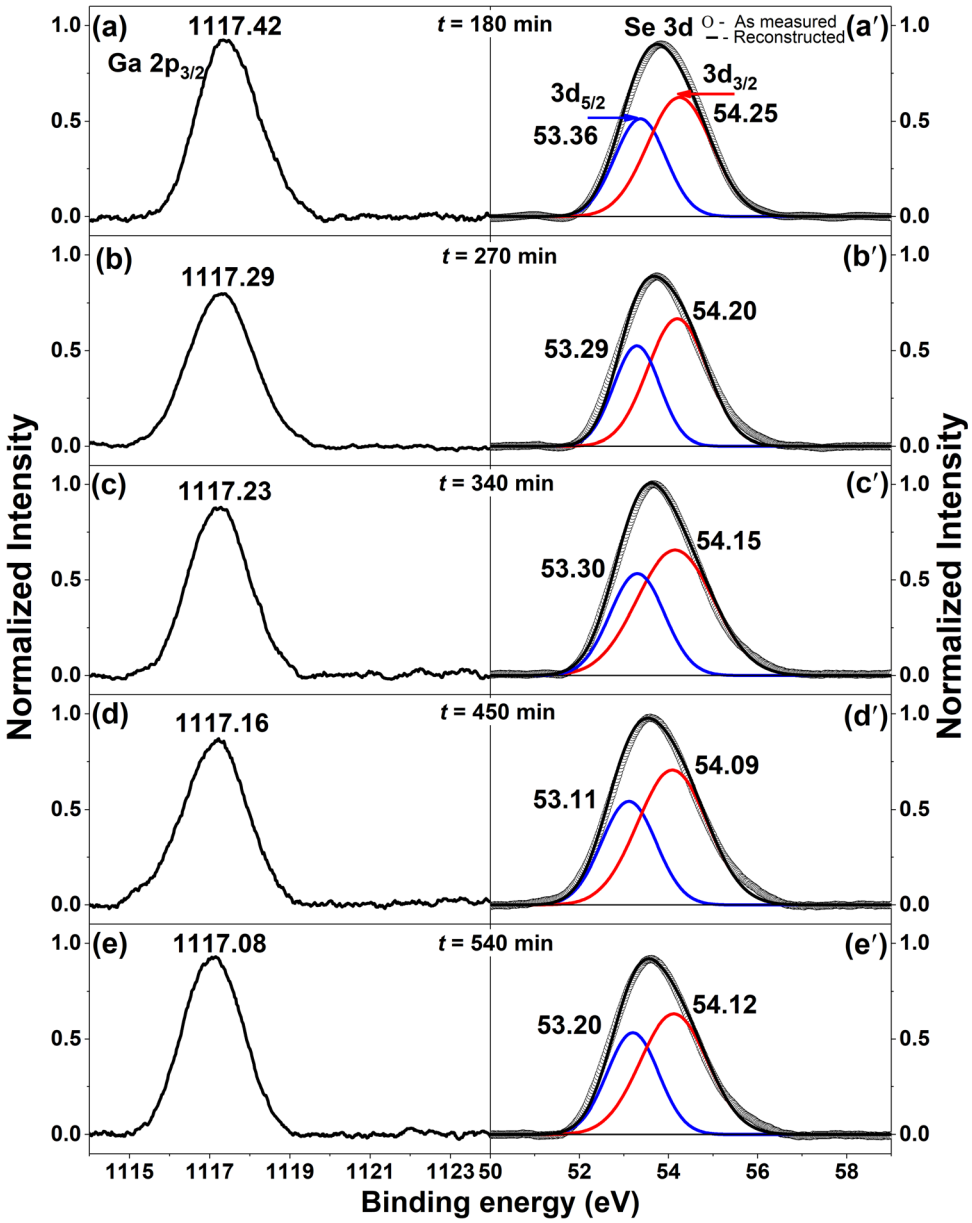

Fig. 7 Core level XPS spectra of **a**–**e** Ga 2p and **a′**–**e′** Se 3d for the CIGS films deposited on the soda lime glass substrates by varying deposition time from 180 to 540 min using RF magnetron sputtering

Table 1 Elemental binding energy positions of Cu 2p, In 3d, Ga 2p, and Se 3d peaks as resolved from the XPS spectrum for the CIGS films deposited on the soda lime glass substrates by varying deposition time from 180 to 540 min using RF magnetron sputtering

Deposition time (min)	Binding energy positions as resolved from XPS						
	Cu $2p_{3/2}$	Cu $2p_{1/2}$	In $3d_{5/2}$	In $3d_{3/2}$	Ga $2p_{3/2}$	Se $3d_{5/2}$	Se $3d_{3/2}$
180	931.85	951.53	444.40	451.98	1117.42	53.36	54.25
270	931.78	951.50	444.30	451.85	1117.29	53.29	54.20
360	931.68	951.45	444.26	451.80	1117.23	53.30	54.15
450	931.65	951.44	444.20	451.72	1117.16	53.11	54.09
540	931.63	951.42	444.13	451.68	1117.08	53.20	54.12

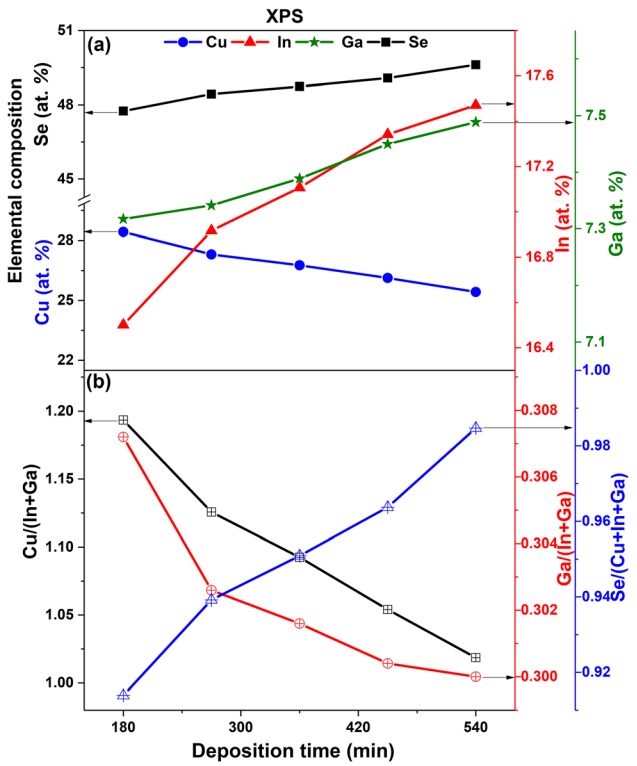

Fig. 8 Elemental composition as measured using XPS of **a** variation in chemical composition and **b** Element ratio of Cu/(In + Ga), Ga/(In + Ga), and Se/(Cu + In + Ga) for the CIGS films deposited on the soda lime glass substrates by varying deposition time from 180 to 540 min using RF magnetron sputtering

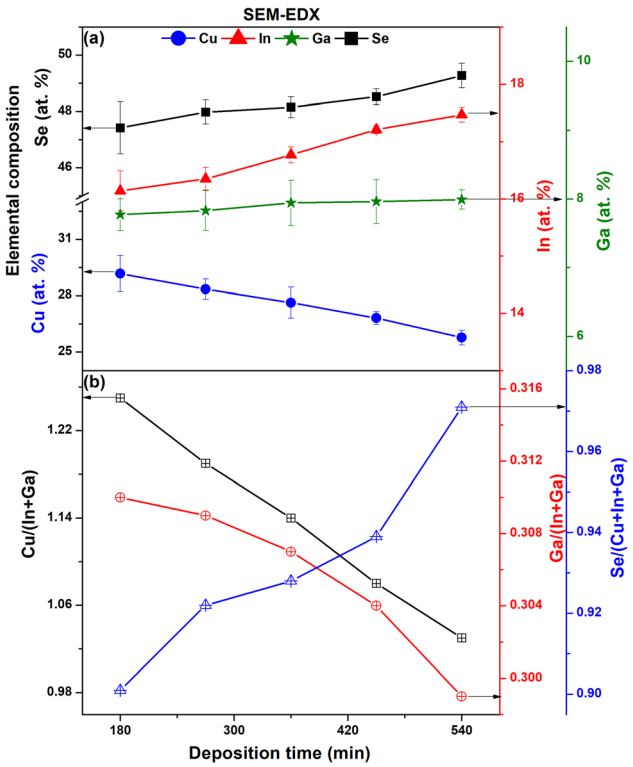

Fig. 9 Elemental composition as measured using SEM–EDS of **a** variation in chemical composition and **b** Element ratio of Cu/(In + Ga), Ga/(In + Ga), and Se/(Cu + In + Ga) for the CIGS films deposited on the soda lime glass substrates by varying deposition time from 180 to 540 min using RF magnetron sputtering

increase in the concentration of In and Se along with a decrease in the quantities of Cu and overall Ga (i.e., Ga/(In + Ga)), thereby bringing a transition in the film from semi-metallic to semiconductor type (see Table 2). Note that, the target was Cu-rich, which means even though sputter yield of Cu is lower than that of In, initially, during the sputter deposition process, the film composition became high in Cu (than In), which gradually reversed with increasing deposition time (i.e., film thickness) because of the depletion of Cu from the target surface along with

Table 2 Elemental compositions as measured by XPS and SEM–EDS along with their corresponding Cu/(In + Ga), Ga/(In + Ga) and Se/M (i.e., M = (Cu + In + Ga)) atomic ratios for the CIGS films deposited on the soda lime glass substrates by varying deposition time from 180 to 540 min using RF magnetron sputtering

Deposition time (min)	XPS						SEM–EDX					
	Cu (at. %)	In (at. %)	Ga (at. %)	Se (at. %)	Cu/(In + Ga)	Ga/(In + Ga)	Se/M	Cu (at. %)	In (at. %)	Ga (at. %)	Se (at. %)	Cu/(In + Ga)	Ga/(In + Ga)	Se/M
180	28.43	16.50	7.32	47.75	1.19	0.307	0.914	29.17 ± 0.97	16.14 ± 0.35	7.27 ± 0.23	47.42 ± 0.92	1.25	0.310	0.901
270	27.30	16.91	7.34	48.44	1.13	0.303	0.939	28.34 ± 0.54	16.35 ± 0.20	7.33 ± 0.29	47.98 ± 0.43	1.19	0.309	0.922
360	26.76	17.11	7.39	48.74	1.09	0.302	0.951	27.63 ± 0.83	16.77 ± 0.14	7.44 ± 0.33	48.15 ± 0.37	1.14	0.307	0.928
450	26.13	17.34	7.45	49.08	1.05	0.300	0.964	26.81 ± 0.34	17.21 ± 0.07	7.46 ± 0.32	48.52 ± 0.28	1.08	0.304	0.939
540	25.43	17.47	7.49	49.62	1.02	0.300	0.985	25.77 ± 0.39	17.48 ± 0.13	7.49 ± 0.14	49.27 ± 0.43	1.03	0.299	0.971

higher sputter yield of In (see Figs. 8, 9 and Table 2) [41, 82]. At the end of 540 min, the film composition nearly assumed the target composition.

The optical band gap (E_g) for these films was calculated from the intercept of the linear portion of $(\alpha h\nu)^2$ vs. $(h\nu)$ plots on X-axis (i.e., energy axis) using the following Tauc equation (see Fig. 10a) [83, 84]

$$(\alpha h\nu) = C(h\nu - E_g)^n, \tag{5}$$

where α is the calculated absorption coefficient from the measured transmission spectra, ν is the frequency of radiation, h is the Planck's constant, C is constant and $n = 1/2$ is for direct transition. The calculated α from the transmittance spectra showed more than 10^5 cm^{-1} for all these films in the entire wavelength range considered here. E_g was found to decrease from 1.32 to 1.16 eV with increasing film thickness and decreasing Ga/(In + Ga)-ratio (i.e., by increasing t from 180 to 540 min, which altered the Ga/(In + Ga)-ratio from 0.307 to 0.300; see Figs. 8, 9, and 10b, Tables 2 and 3), which was well within the range of the CIGS films reported in the literature [68]. Adel et.al. had deposited the CIGS films using the electrodeposition route on ITO coated glass substrates, followed by 30 min annealing at 350 °C in nitrogen atmosphere. They had observed bandgap reduction with decreasing Ga/(In + Ga)-ratio, which is in agreement with our results [85]. The decrease in E_g could be associated to the decrease in the donor-related electronic defect states (or) trap states, which occurred at higher film thicknesses (see above). In this regard, Prepelita et.al. had observed a decrease in the optical band gap in the CIGS films as a function of varying thickness in the range of 750 to 1200 nm, and had attributed to the changes in chemical composition of these films [86]. Mishra et al. had fabricated CIGS films by varying the film thickness in the range of 466 and 1700 nm in RF magnetron sputtering, in which E_g of CIGS thin films was found to decrease from 1.23 to 1.12 eV with the increases in the film thickness [56]. Chihi et.al. have also reported similar types of results by using the electrodeposition technique, in which E_g decreased from 1.42 to 1.24 eV with the increases in the film thickness from 855 to 1100 nm [49]. Note here that, they had performed the annealing treatment on these as-deposited films in argon atmosphere at 400 °C for 30 min, which is higher than the deposition temperature used in our study (i.e., 250 °C). The transport gap of these semiconductor-type films as calculated in this study using

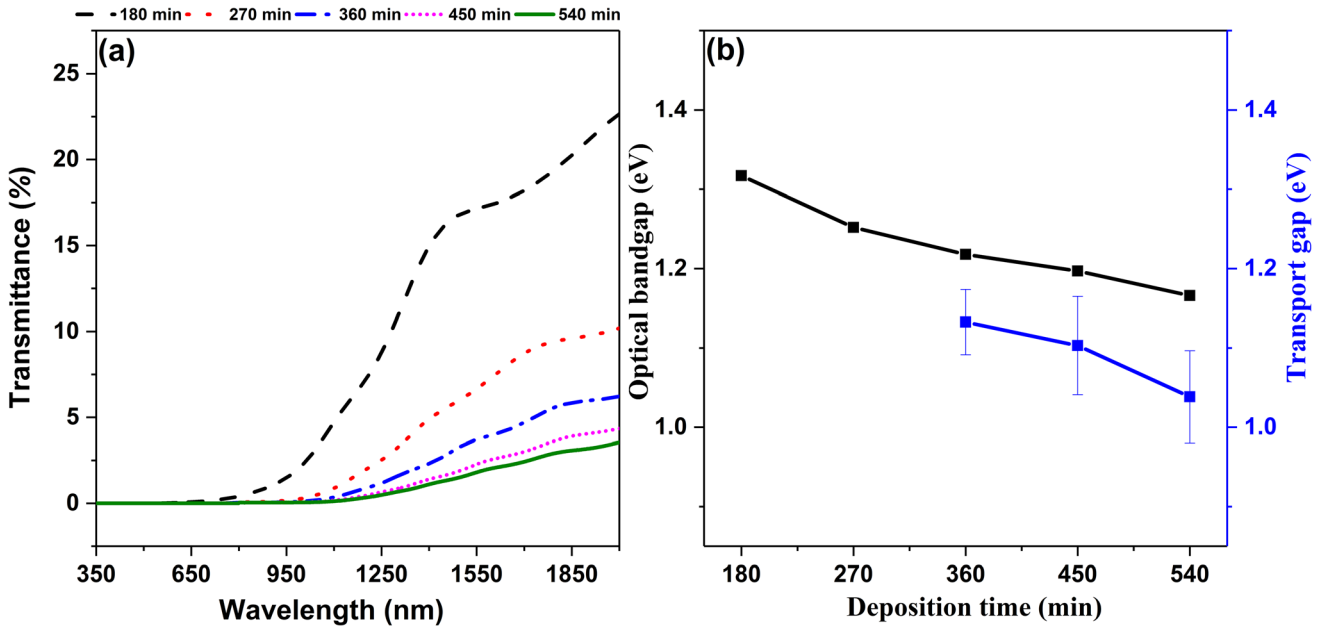

Fig. 10 **a** Optical transmittance spectra and **b** Optical band gap and average transport gap for the CIGS films deposited on the soda lime glass substrates by varying deposition time from 180 to 540 min using RF magnetron sputtering

Table 3 Positions of the conduction band edge, valence band edge, average transport gap as measured using STM/STS and optical band gap as measured using UV–Vis-NIR spectrophotometer for the CIGS films deposited on the soda lime glass substrates by varying deposition time from 180 to 540 min using RF magnetron sputtering

Deposition time (min)	Conduction band position (eV)	Valence band position (eV)	Avg. transport gap (eV)	Optical band gap (eV)
180	–	–	–	1.32
270	–	–	–	1.25
360	0.77 ± 0.04	− 0.36 ± 0.03	1.13 ± 0.04	1.22
450	0.72 ± 0.06	− 0.39 ± 0.03	1.10 ± 0.06	1.19
540	0.64 ± 0.05	− 0.40 ± 0.05	1.04 ± 0.06	1.16

STM/STS was also found to follow the trend of E_g (see Fig. 10b).

Refractive index (n) of these films was calculated from the interference fringes of the optical reflectance spectra by using the following equation (see Fig. 11) [87, 88].

$$n = \frac{\lambda_1 \lambda_2}{2.x.(\lambda_2 - \lambda_1)}, \quad (6)$$

where λ_1 and λ_2 are the two adjacent reflectance maxima of the interference fringes and x is the thickness of the films. n for these films was found in the range of 2.17–2.91 (see Table 4). Note that, only one n data has been reported here for the thinnest film (i.e., film deposited at t of 180 min), because of absence of the sufficient number of interference fringes in the reflectance spectra [89, 90]. With increasing CIGS film thickness, μ_h was found to increase from 0.03 to 8.86 cm^2/V-s (see Fig. 4), which could be associated to the reduction in electron scattering because of an overall decrease in the grain boundary area, number of holes, and overall donor- and acceptor-types of electronic defect densities. As a result, ρ for these films increased from 0.66 to 3.22 Ω·cm with increasing film thickness (as t increased from 180 to 540 min). Note that, ρ is related to p_h and μ_h as per the following equation:

$$\rho = \frac{1}{p_h.e.\mu_h}, \quad (7)$$

where e is the electronic charge.

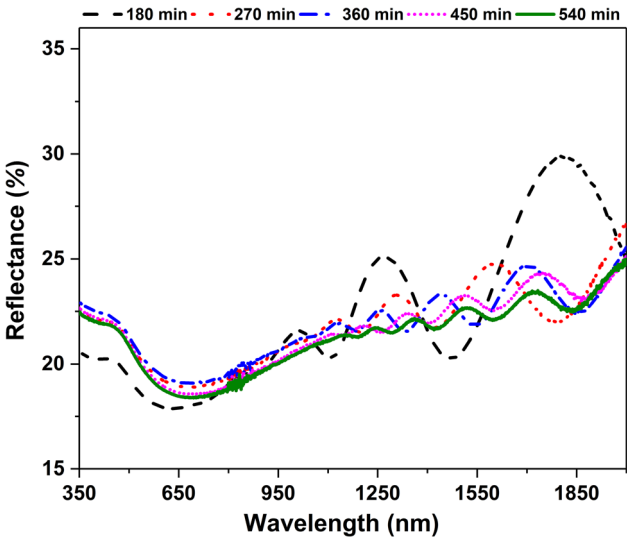

Fig. 11 Reflectance spectra in the range of 350–2000 nm for the CIGS films deposited on the soda lime glass substrates by varying deposition time from 180 to 540 min using RF magnetron sputtering

Table 4 Refractive indices as measured using UV–Vis-NIR spectrophotometer for the CIGS films deposited on the soda lime glass substrates by varying deposition time from 180 to 540 min using RF magnetron sputtering

Deposition time (min)	Average film thickness x (nm)	$\lambda 1$ (nm)	$\lambda 2$ (nm)	$\lambda 3$ (nm)	$\lambda 4$ (nm)	$\lambda 5$ (nm)	Adjacent wavelengths	Refractive index (n)
180	901	1012	1268	–-	–-	–-	$\lambda 2$, $\lambda 1$	2.78
270	1350	1125	1313	1601	–-	–-	$\lambda 2$, $\lambda 1$	2.91
							$\lambda 3$, $\lambda 2$	2.70
360	1802	1121	1256	1446	1705	–-	$\lambda 2$, $\lambda 1$	2.89
							$\lambda 3$, $\lambda 2$	2.65
							$\lambda 4$, $\lambda 3$	2.64
450	2357	1111	1210	1341	1507	1753	$\lambda 2$, $\lambda 1$	2.88
							$\lambda 3$, $\lambda 2$	2.63
							$\lambda 4$, $\lambda 3$	2.58
							$\lambda 5$, $\lambda 4$	2.28
540	2845	1151	1244	1361	1520	1733	$\lambda 2$, $\lambda 1$	2.71
							$\lambda 3$, $\lambda 2$	2.54
							$\lambda 4$, $\lambda 3$	2.29
							$\lambda 5$, $\lambda 4$	2.17

Note that the wavelengths i.e., λ_1, λ_2, λ_3, λ_4 and λ_5 are the reflectance maxima of the interference fringes

In the present work, the CIGS film deposited at t of 540 min, was found to yield a film thickness of about 2.85 µm, with p_h of 2.17×10^{17} cm^{-3} and E_g of 1.16 eV; optoelectronic properties that are suitable as an absorber layer for photovoltaic application.

4 Conclusion

In this work, thickening CIGS films were deposited by varying the deposition time from 180 to 540 min on soda lime glass substrates in RF magnetron sputtering. Here a single step deposition and by use of a single quaternary CIGS target was employed. Moreover, the substrate temperature was kept lower (i.e., of 523 K) to deposit these thickening films. A range of surface and bulk characterization techniques were then used to investigate the microstructure, bulk optoelectronic, and surface electrical properties of these films. All these films were found to grow in single phase, chalcopyrite crystal structure, and with dominant (112) orientation. Moreover, CIGS film was found to make from a semimetallic to semiconductor transition with increasing film thickness that was

correlated with the variation in the type, quantities and position of the intrinsic electronic defect states and also to the hole concentrations in these films. Optical band gap was found to decrease from 1.32 to 1.16 eV with increasing film thickness because of a change in film composition. The refractive index of these films was found to be in the range of 2.17–2.91. Moreover, CIGS film deposited for 540 min was found to yield a film thickness of about 2.85 µm, with hole concentration of 2.17×10^{17} cm^{-3} and optical band gap of 1.16 eV; optoelectronic properties that are appropriate for an absorber layer in photovoltaic application. Thus, in this work, a facile, cost-effective deposition technique for the growth of CIGS film was developed, where a relatively lower substrate temperature was used. As a next step, this technique can be employed in fabricating a CIGS-based solar cell device.

Acknowledgements

We gratefully acknowledge financial support from Science and Engineering Research Board (SERB), Department of Science and Technology, Government of India (Project No: EMR/2016/001182). Further, we would like to thank Professor Gouthama (Advanced Centre for Materials Science (ACMS), IIT Kanpur, India) for X-ray photoelectron spectroscopy measurement.

Declarations

Conflict of interest The authors declare no conflicts of interest.

References

1. F. Kang, J. Ao, G. Sun, Q. He, Y. Sun, J. Alloys Compd. **478**, 2008 (2009)
2. G. Hanna, A. Jasenek, U. Rau, H.W. Schock, Thin Solid Films **387**, 71 (2001)
3. K.L. Chopra, P.D. Paulson, V. Dutta, Renew. Energy. **8**, 69 (1996)
4. M. Powalla, B. Dimmler, R. Schaeffler, G. Voorwinden, U. Stein, H.D. Mohring, F. Kessler, and D. Hariskos, In: Proceeding of the 19th European Photovoltaic Solar Energy Conference 1663 (2004).
5. M. Powalla, B. Dimmler, Sol. Energy Mater. Sol. Cells. **67**, 337 (2001)
6. H.J. Möller, *Semiconductors for Solar Cells* (Artech House. Inc, Norwood, 1993)
7. C.-S. Jiang, M.A. Contreras, I. Repins, H.R. Moutinho, Y. Yan, M.J. Romero, L.M. Mansfield, R. Noufi, M.M. Al-Jassim, Appl. Phys. Lett. **101**, 33903 (2012)
8. M. Raghuwanshi, B. Thöner, P. Soni, M. Wuttig, R. Wuerz, O. Cojocaru-Mirédin, A.C.S. Appl, Mater. Interfaces. **10**, 14759 (2018)
9. M. Green, E. Dunlop, J. Hohl-Ebinger, M. Yoshita, N. Kopidakis, X. Hao, Prog. Photovoltaics Res. Appl. **29**(1), 3–15 (2021)
10. M Nakamura, K Yamaguchi, Y Kimoto, Y Yasaki, T Kato, H Sugimoto, 46th IEEE PVSC (2019).
11. J. Ramanujam, U.P. Singh, Energy Environ. Sci. **10**(6), 1306 (2017)
12. Z. Li, H. Qing, J. Wei-Long, L. Chang-Jian, S. Yun, Chin. Phys. Lett. **25**(2), 734 (2008)
13. N.G. Dhere, S.R. Ghongadi, M.B. Pandit, A.H. Jahagirdar, D. Scheiman, Prog. Photovolt: Res. Appl. **10**(6), 407 (2002)
14. M. Kaelin, D. Rudmann, A.N. Tiwari, Sol. Energy **77**(6), 749 (2004)
15. W. Li, X. Yan, A.G. Aberle, S. Venkataraj, Sci. Rep. **9**(1), 2637 (2019)
16. J. Jean, P.R. Brown, R.L. Jaffe, T. Buonassisi, V. Bulović, Energy Environ. Sci. **8**(4), 1200 (2015)
17. D. Yokoyama, T. Minegishi, K. Maeda, M. Katayama, J. Kubota, A. Yamada, M. Konagai, K. Domen, Electrochem. Commun. **12**(6), 851 (2010)
18. T.J. Jacobsson, V. Fjällström, M. Edoff, T. Edvinsson, Sol. Energy Mater. Sol. Cells **134**, 185 (2015)
19. R.C. Valderrama, P.J. Sebastian, J.P. Enriquez, S.A. Gamboa, Sol. Energy Mater. Sol. Cells **88**(2), 145 (2005)
20. X. Zhu, C.W. Liu, Appl. Phys. Lett. **105**(14), 143502 (2014)
21. J. Gong, Y. Kong, J. Li, K. Wang, X. Wang, Z. Zhang, Z. Ding, X. Xiao, Nano Energy **62**, 205 (2019)
22. H. Heriche, Z. Rouabah, N. Bouarissa, Optik **127**(24), 11751 (2016)
23. S. Yoshiba, M. Hirai, Y. Abe, M. Konagai, Y. Ichikawa, AIP Adv. **7**(2), 025104 (2017)
24. M.N. Harif, S.F. Abdullah, A.W.M. Zuhdi, F. Za'Abar, M.S. Bahrudin and A.H. Hasani, IEEE 201 (2018).
25. S. Furue, S. Ishizuka, A. Yamada, M. Iioka, H. Higuchi, H. Shibata, S. Niki, Sol. Energy Mater. Sol. Cells **119**, 163 (2013)
26. H. Mönig, R. Caballero, C.A. Kaufmann, T.L. Schmidt, M.C. Lux-Steiner, S. Sadewasser, Sol. Energy Mater. Sol. Cells. **95**, 1537 (2010)
27. S. Bröker, D. Kück, A. Timmer, I. Lauermann, B. Ümsür, D. Greiner, C.A. Kaufmann, H. Mönig, A.C.S. Appl, Mater. Interfaces. **7**, 13062 (2015)

28. B. Kundu, A.J. Pal, J. Appl. Phys. **122**, 065109 (2017)
29. C.S. Jiang, R. Noufi, J.A. AbuShama, K. Ramanathan, H.R. Moutinho, J. Pankow, M.M. Al-Jassim, Appl. Phys. Lett. **84**(18), 3477 (2004)
30. M.A. Green, Y. Hishikawa, E.D. Dunlop, D.H. Levi, J. Hohl-Ebinger, A.W.Y. Ho-Baillie, Prog Photovolt Res Appl. **26**, 427 (2018)
31. M.A. Contreras, B. Egaas, K. Ramanathan, J. Hiltner, A. Swartzlander, F. Hasoon, R. Noufi, Prog. Photovoltaics Res. Appl. **7**, 311–316 (1999)
32. V.K. Kapur, A. Bansal, P. Le, O.I. Asensio, Thin Solid Films **431**, 53–57 (2003)
33. H.K. Song, S.G. Kim, H.J. Kim, S.K. Kim, K.W. Kang, J.C. Lee, K.H. Yoon, Sol. Energy Mater. Sol. Cells. **75**, 145–153 (2003)
34. S.C. Chen, D.H. Hsieh, H. Jiang, Y.K. Liao, F.I. Lai, H. Chen, H.C. Kuo, Nanoscale Res Lett. **9**(1), 1–7 (2014)
35. M.A. Hossain, Z. Tianliang, L.K. Keat, L. Xianglin, R.R. Prabhakar, S.K. Batabyal, L.H. Wong, J. Mater. Chem. A **3**(8), 4147–4154 (2015)
36. Y. Lian, J. Shanshan, L. Zhao, J. Zhang, P. Yang, J. Zhang, M. An, New J. Chem. **39**, 7742–7745 (2015)
37. S. Jung, S. Ahn, J.H. Yun, J. Gwak, D. Kim, K. Yoon, Curr. Appl. Phys. **10**(4), 990–996 (2010)
38. C. Adel, B.M. Fethi, B. Brahim, J. Mater. Sci. **27**(4), 3481–3487 (2016)
39. H. Lee, H. Yoon, C. Ji, D. Lee, J.H. Lee, J.H. Yun, Y. Kim, J. Electron. Mater. **41**(12), 3375–3381 (2012)
40. V. Bermudez, Sol. Energy **175**, 2–8 (2018)
41. Z. Yu, C. Yan, T. Huang, W. Huang, Y. Yan, Y. Zhang, L. Liu, Y. Zhang, Y. Zhao, Appl. Surf. Sci. **258**, 5222 (2012)
42. M. Marudachalam, H. Hichri, R. Klenk, R.W. Birkmire, W.N. Shafarman, J.M. Schultz, Appl. Phys. Lett. **67**, 3978 (1995)
43. I. Repins, M.A. Contrers, B. Egaas, C. DeHart, J. Scharf, C.L. Perkins, B. To, R. Noufi, Prog. Photovolt **16**, 235 (2008)
44. S. Seike, K. Shiosaki, M. Kuramoto, H. Komaki, K. Matsubara, H. Shibata, S. Ishizuka, A. Yamada, S. Niki, Sol. Energy Mater. Sol. Cells. **95**, 254 (2011)
45. Y.C. Lin, J.H. Ke, W.T. Yen, S.C. Liang, C.H. Wu, C.T. Chiang, Appl. Surf. Sci. **257**, 4278 (2011)
46. J. Kim, H.S. Lee, N.M. Park, Curr. Appl. Phys. **14**, S63 (2014)
47. H. Wang, Y. Zhang, X.L. Kou, Y.A. Cai, W. Liu, T. Yu, J.B. Pang, C.J. Li, Y. Sun, Semicond. Sci. Technol. **25**, 055007 (2010)
48. Y.T. Hsu, K.F. Huang, S.I. Tsai, W.H. Lan, M. Yueh, J.C. Lin, K.J. Chang, W.J. Lin, Proc. SPIE. **8470**, 1 (2012)
49. A. Chihi, B. Bessais, J. Electron. Mater. **46**, 354 (2017)
50. S.M. Kong, R. Fan, S.H. Jung, C.W. Chung, J. Ind. Eng. Chem. **19**, 1320 (2013)
51. T. Schlenker, M.L. Valero, H.W. Schock, J.H. Werner, J. Cryst. Growth **264**, 178 (2004)
52. Y. Zhou, Y. Yan, S. Li, Y. Zhang, C. Yan, L. Liu, Y. Zhang, Y. Zhao, Appl. Surf. Sci. **264**, 197–201 (2013)
53. J. Müller, J. Nowoczin, H. Schmitt, Thin Solid Films **496**(2), 364–370 (2006)
54. L. Zhang, Q. He, W.L. Jiang, F.F. Liu, C.J. Li, Y. Sun, Solar Energy Mater. Solar Cells **93**(1), 114–118 (2009)
55. C. Singh, E. Panda, RSC Adv. **6**, 48910 (2016)
56. P.K. Mishra, J.N. Prasad, V. Dave, R. Chandra, A.K. Choudhary, Mater. Sci. Semicond. Process. **34**, 350 (2015)
57. R. Feenstra, J. Stroscio, A. Fein, Surf. Sci. **181**, 295 (1987)
58. S. Kano, T. Tada, Y. Majima, Chem. Soc. Rev. **44**, 970 (2015)
59. N.D. Lang, Phys. Rev. B. **34**, 5947 (1986)
60. C.C. Singh, T.A. Patel, E. Panda, J. Appl. Phys. **117**, 245312 (2015)
61. C.C. Singh, E. Panda, J. Appl. Phys. **123**, 174904 (2018)
62. B. Ghosh, A.J. Pal, J. Appl. Phys. **110**(10), 104303 (2011)
63. H. Mönig, R. Caballero, C.A. Kaufmann, T.L. Schmidt, MCh. Lux-Steiner, S. Sadewasser, Sol. Energy Mater. Sol. Cells **95**(6), 1537–1543 (2011)
64. S. Chakrabarti, A.J. Pal, Nanoscale **7**(21), 9886–9893 (2015)
65. S.B. Zhang, S.H. Wei, A. Zunger, H.K. Yoshida, Phys. Rev. B. **57**, 9642 (1998)
66. U. Rau, H.W. Schock, Appl. Phys. A. **69**, 131 (1999)
67. E. Korhonen, K. Kuitunen, F. Tuomisto, A. Urbaniak, M. Igalson, J. Larsen, L. Gütay, S. Siebentritt, Y. Tomm, Phys. Rev. B **86**, 064102 (2012)
68. S. Siebentritt, Thin Solid Films **403**, 1 (2002)
69. S. Siebentritt, Curr. Opin. Green Sustain. Chem. **4**, 1 (2017)
70. A. Bera, S.K. Sahaa, A.J. Pal, Nanoscale **7**(41), 17366–17374 (2015)
71. S. Broker, D. Kück, A. Timmer, I. Lauermann, B. Ümsür, D. Greiner, H. Mönig, ACS Appl. Mater. Interfaces. **7**(23), 13062–13072 (2015)
72. W. Li, Y. Ma, S. Yang, J. Gong, S. Zhang, X. Xiao, Nano Energy **33**, 157–167 (2017)
73. C. Caldero, P.B. Perez, O. Rodriguez, G. Gordillo, Microelectronics J. **39**, 1324 (2008)
74. C.D. Wagner, W.M. Riggs, L.E. Davis, J.F. Moulder, and G.E. Muilenberg, Handbook of X- Ray Photoelectron Spectroscopy, Perkin-Elmer, Co., Minnesota (1979).
75. D. Cahen, P.J. Ireland, L.L. Kazmerski, F.A. Thiel, J. Appl. Phys. **57**, 4761 (1984)
76. L.L. Kazmerski, O. Jamjoum, P.J. Ireland, S.K. Deb, R.A. Mickelsen, W. Chen, J. Vac. Sci. Technol. **19**, 467 (1981)
77. D. Schmid, M. Ruckh, H.W. Schock, Appl. Surf. Sci. **103**, 409 (1996)
78. S. Evans, Surf. Interface Anal. **7**, 299 (1985)

79. S. Marsillac, J.C. Bernede, R. Le Ny, A. Conan, Pergamon. **46**, 1315 (1995)
80. H.I. Hsiang, C.T. Yang, J.H. Tu, RSC Adv. **6**, 99297 (2016)
81. Y. Qiu, C. Leung, S. Yang, L. Wang, T.-C. Lau, G. Liu, Appl. Catal. A **402**, 23 (2011)
82. F.O. Adurodija, J. Song, S.D. Kim, S.H. Kwon, S.K. Kim, K.H. Yoon, B.T. Ahn, Thin Solid Films **338**, 13 (1999)
83. Z. Yu, Y. Yan, S. Li, Y. Zhang, C. Yan, L. Liu, Y. Zhang, Y. Zhao, Appl. Surf. Sci. **264**, 197 (2013)
84. Y.C. Lin, W.T. Yen, Y.L. Chen, L.Q. Wang, F.W. Jih, Phys. B. **406**, 824 (2011)
85. C. Adel, B.M. Fethi, B. Brahim, Appl. Phys. A **122**(2), 62 (2016)
86. P. Prepelita, I. Stavarache, C. Negrila, F. Garoi, V. Craciun, Appl. Surf. Sci. **424**, 421–427 (2017)
87. R. Swanepoel, J. Phys. E **16**, 1214 (1983)
88. Z. Yu, C. Yan, Y. Yan, Y. Zhang, T. Huang, W. Huang, S. Li, L. Liu, Y. Zhang, Y. Zhao, Appl. Surf. Sci. **258**, 8527 (2012)
89. D. Poelman, P.F. Smet, J. Phys. D **36**, 1850 (2003)
90. A.M. Nasr, H.I.A. El-Kader, M. Farhat, Thin Solid Films **515**, 1758 (2006)